Nanoscale

COMMUNICATION

View Article Online
View Journal | View Issue

Cite this: *Nanoscale*, 2021, **13**, 13617

Received 23rd June 2021,
Accepted 29th July 2021

DOI: 10.1039/d1nr04080d

rsc.li/nanoscale

Benchmarking atomically defined AFM tips for chemical-selective imaging†

Bertram Schulze Lammers,[a,b] Damla Yesilpinar,[a,b] Alexander Timmer,[b] Zhixin Hu, *[c] Wei Ji, [d] Saeed Amirjalayer, [a,b,e] Harald Fuchs [a,b] and Harry Mönig *[a,b]

Controlling the identity of the tip-terminating atom or molecule in low-temperature atomic force microscopy has led to ground breaking progress in surface chemistry and nanotechnology. Lacking a comparative tip-performance assessment, a profound standardization in such experiments is highly desirable. Here we directly compare the imaging and force-spectroscopy capabilities of four atomically defined tips, namely Cu-, Xe-, CO-, and O-terminated Cu-tips (CuOx-tips). Using a nanostructured copper-oxide surface as benchmark system, we found that Cu-tips react with surface oxygen, while chemically inert Xe- and CO-tips allow entering the repulsive force regime enabling increased resolution. However, their high flexibility leads to imaging artifacts and their strong passivation suppresses the chemical contrast. The higher rigidity and selectively increased chemical reactivity of CuOx-tips prevent tip-bending artifacts and generate a distinct chemical contrast. This result is particularly promising in view of future studies on other metal–oxide surfaces.

Introduction

Functionalizing the probe tip of an atomic force microscope (AFM) with inert probe particles, constitutes a milestone for structural,[1–4] mechanical,[5,6] and chemical[7–12] investigations of surfaces and adsorbates on the atomic scale. In particular, the chemical passivation of the metallic tip apex is the key for imaging at reduced tip–sample distances, where the short-range Pauli-repulsion dominates the contrast, leading to a drastically increased resolution.[3,13–16] Imaging at such close distances is usually achieved in the noncontact (NC-) AFM mode with a tuning-fork based cantilever in the qPlus configuration.[17] This force sensor enables oscillation amplitudes down to the sub-ångström regime where the atomic tip–surface interaction is reflected in a frequency shift Δf with respect to its free resonance frequency.

The most common approaches to functionalize a metallic tip apex are picking up a single CO molecule, a Xe atom or an organic molecule, from the surface under study.[13,18–21] Despite its tremendous success, a major limitation of this approach is related to the weak coupling between the probe particles and the metallic tip base. In fact, it leads to a dynamic bending of the probe particles during surface scanning in the Pauli repulsion regime. This results in image distortions and a related systematic over-estimation of bond lengths within organic nano-structures.[7,22–24] In addition, such tip flexibility is particularly problematic at sites with strongly varying tip–sample potential (*e.g.* at intermolecular sites) where the dynamic bending can lead to artificial contrast signatures.[7,20,23–26]

In recent years, oxygen-terminated copper (CuOx-) tips emerged as an alternative approach for tip functionalization.[24,27–30] Here, the oxygen atom is covalently bound within a tetrahedral configuration to the copper base of the tip. Consequently, CuOx-tips are considerably more rigid as compared to the approaches involving the weakly attached probe particles.[31] While recent studies on various organic molecules demonstrated that this significantly reduces the mentioned artifacts, a direct comparison of different tips in one benchmark experiment is pending. Moreover, given the huge potential of tip functionalization approaches toward standardized scanning probe microscopy experiments, this methodology should increasingly be exploited to inorganic sample systems.[26,32]

In the present study we compared the performance of four atomically defined probe-tip terminations (1) metallic Cu-, (2) CO-, (3) Xe-, and (4) CuOx-tips. For our investigations we used a partially oxidized Cu(110) surface exhibiting alternating

[a]*Physikalisches Institut, Westfälische Wilhelms-Universität, 48149 Münster, Germany. E-mail: harry.moenig@uni-muenster.de*
[b]*Center for Nanotechnology, 48149 Münster, Germany*
[c]*Center for Quantum Joint Studies and Department of Physics, Tianjin University, Tianjin, China. E-mail: zhixin.hu@tju.edu.cn*
[d]*Department of Physics and Beijing Key Laboratory of Optoelectronic Functional Materials & Micro-Nano Devices, Renmin University of China, Beijing, China*
[e]*Center for Multiscale Theory and Computation, 48149 Münster, Germany*
†Electronic supplementary information (ESI) available. See DOI: 10.1039/d1nr04080d

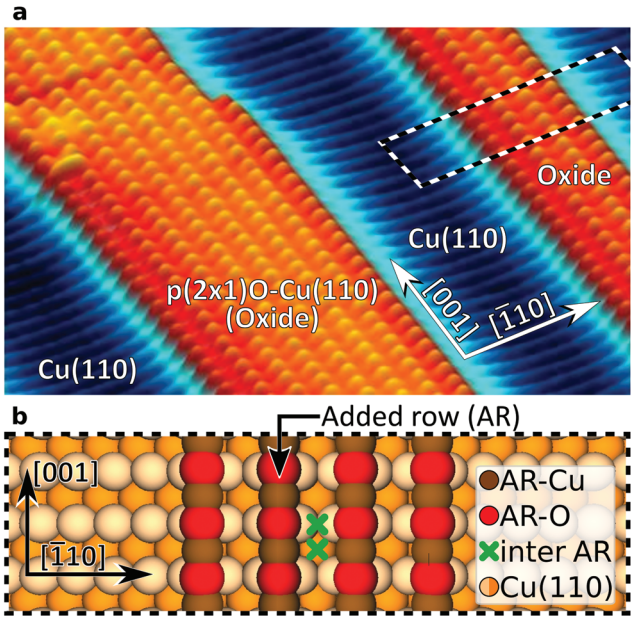

Fig. 1 Atomic structure of a partially oxidized Cu(110) surface. (a) Constant frequency-shift AFM image of two protruding p(2 × 1)O–Cu (110)-reconstructed oxide stripes (orange) separated by bare Cu(110) areas (blue). (b) Atomistic model of an oxide stripe with four added rows corresponding to the area marked by the dashed box in (a). The green crosses mark distinct atomic sites between the ARs.

stripes of bare Cu(110) and typical (2 × 1)O-reconstructed oxide stripes on top[33] as model system (Fig. 1). Due to the strongly varying electrostatic potential on the alternating copper (AR-Cu) and oxygen (AR-O) atoms in such added rows (ARs), this surface provides an ideal structure to challenge the imaging- and site-selective force-spectroscopy performance of the compared tips. For each tip we performed height-dependent imaging, complemented by a spectroscopic analysis of the AFM contrast. Our results are supported by mechanistic simulations[20] to examine the effect of tip flexibility. To gain detailed knowledge on the influence of the tip-terminating atom on chemical interaction within the tip–sample junction, density functional theory (DFT) was applied.

Experimental

We used a low-temperature scanning probe microscopy (SPM) system from Scienta Omicron (LT-STM/AFM). It was operated under ultrahigh-vacuum conditions with a base pressure below 5×10^{-11} mbar and cooled by a liquid-helium bath cryostat to ~5 K. The experiments were performed with the MATRIX SPM control system and with commercial qPlus force sensors.[17,34] The sensor resonance frequencies f_0 were between 24 and 28 kHz with quality factors in a range of 10k–50k. This set-up enables simultaneous STM and AFM data recording with electro-chemically etched tungsten tips.

The AFM experiments were performed with an active constant-amplitude feedback loop and if not otherwise stated, in constant-height mode. As a result, AFM contrast reflects frequency shifts Δf with respect to the resonance frequency f_0 of the free oscillating qPlus sensor. The presented data sets were acquired with three different force sensors. Their specific resonance frequencies and the used scanning parameters are given in the following: Cu-, and Xe-tip data (Fig. 2a and b): f_0 = 24.1 kHz, amplitude 1.0 Å, scanning speed 3 nm s^{-1}; CO-tip data (Fig. 2c): f_0 = 26.7 kHz, amplitude 0.8 Å, scanning speed 4 nm s^{-1}; CuOx-tip results (Fig. 2d): f_0 = 26.7 kHz, amplitude 1.0 Å, scanning speed 5 nm s^{-1}. Overall, we did not observe a direct correlation between these parameters and the noise level. Raw image data are processed with a slight Gaussian filter (Scanning Probe Image Processor, SPIP™5.1). Further experimental and computational details are described in the ESI.†

Results and discussion

Height-dependent contrast analysis

The evolution of the AFM contrast for each tip at decreasing tip-height ΔZ is shown in Fig. 2. Besides the surface structural model below, we also show $\Delta f(Z)$-spectra taken from the most important sites for contrast analysis at the bottom. The pure metallic Cu-tip allows imaging only in the attractive force regime, where the added rows appear as dark vertical lines (Fig. 2a). At the height with the most distinct contrast (ΔZ = 0.0 Å), a slight atomic corrugation can be observed. Any attempt to further reduce ΔZ always leads to sudden tip changes, which we attribute to the high chemical reactivity and related atomic relaxations within the tip–sample junction.[27,35,36] The corresponding $\Delta f(Z)$-spectra (Fig. 2a, bottom) show a clear distinction between the added row (AR-Cu/O) and the topographically lower sites in between (inter AR). However, a chemical identification of the atoms within the added rows is not possible.

The Cu-tip can be chemically passivated by picking up a single xenon atom from the surface.[18,23] Such a Xe-tip allows imaging at considerably smaller tip–sample distances where the Pauli-repulsion dominates the contrast. This results in an increasing frequency shift Δf when the tip is moved closer to the surface. As a consequence, the added rows in Fig. 2b are strongly emphasized as bright continuous lines. By further approaching the surface, the xenon atom starts tilting and the metallic tip base increasingly contributes an attractive interaction. This behavior is particularly reflected in a sudden decrease of the $\Delta f(Z)$-spectra on the added rows at around ΔZ ≈0.7 Å (bottom panel Fig. 2b). The resulting dip-hump evolution of the spectra is a typical feature of a strongly deflected probe particle.[37] As a result of this behavior, the contrast on the added rows becomes less pronounced, which eventually leads to a contrast inversion of added row and inter sites at ΔZ <0.2 Å. This is also represented in the corresponding $\Delta f(Z)$-spectra, where the crossing point indicates the contrast inversion (yellow arrow in Fig. 2b).

A very similar contrast evolution is obtained with a CO-functionalized tip, including the contrast inversion (yellow arrow in

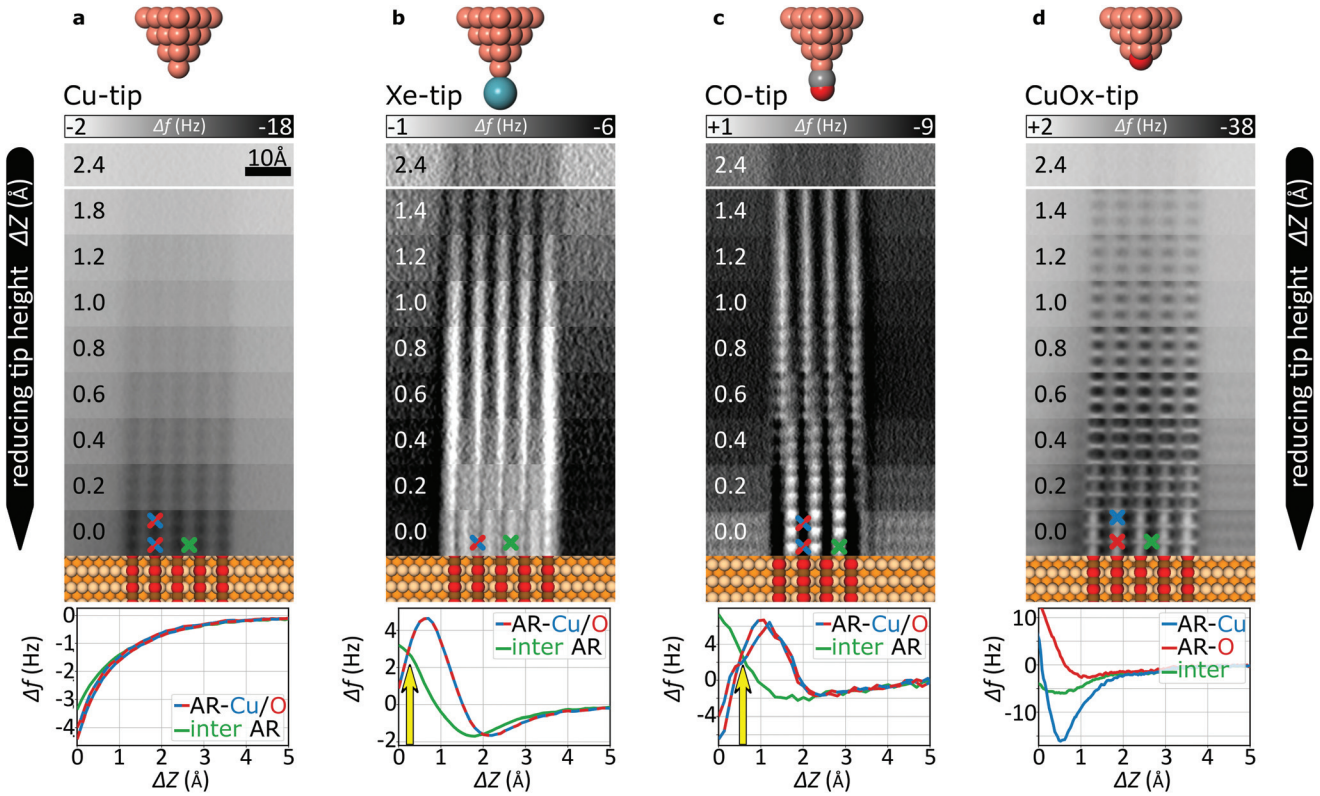

Fig. 2 AFM contrast evolution on oxidized copper stripes. (a) Metallic Cu-tip; (b) Xe-tip; (c) CO-tip; (d) CuOx-tip. Data are recorded in constant-height AFM mode shown for various tip–sample distances, displayed in steps of 0.2 Å and aligned with corresponding structural models. The ΔZ-scale is given in reference to the closest stable frame for each tip. The background-subtracted $\Delta f(Z)$-spectra at the bottom provide further insight in the contrast evolution where the locations of the spectra are indicated by color-coded crosses. The background spectra were taken on the bare Cu (110) area and the yellow arrows mark the tip-height where a contrast inversion occurs.

Fig. 2c). Due to the smaller size of CO as compared to Xe, the contrast appears slightly clearer and indicates some atomic corrugation.

To investigate whether the imaging properties can be improved by using a stiffer tip, we performed the same experiment with the CuOx-tip (Fig. 2d). Imaging an oxide stripe with this tip shows a significantly different contrast evolution (Fig. 2d). For tip heights ΔZ >0.4 Å, the copper atoms within the added rows (AR-Cu) are imaged as dark ellipsoid depressions. In contrast, for tip heights below $\Delta Z \approx 1.0$ Å, the oxygen atoms (AR-O) appear already as bright, localized repulsive features in-between the AR-Cu sites (along the [001]-direction). At ΔZ = 0.2 Å also the surface copper atoms enter the regime where repulsive forces dominate the contrast, *i.e.* the AR-Cu atoms increasingly appear as bright contrast features. Please note that in this regime, potential tip asymmetries would be emphasized in the contrast by the increasingly repulsive interaction (ESI Fig. S1†).

The strongly differing contrast above the AR-Cu and AR-O atoms is reflected in the clear separation of the corresponding $\Delta f(Z)$-spectra at ΔZ <1.5 Å. On the AR-O site, a weak minimum at $\Delta Z \approx 1$ Å is observed, whereas the AR-Cu site shows a distinctly more pronounced minimum at $\Delta Z \approx 0.6$ Å. Furthermore, for small tip heights the spectra continuously approach positive frequency shifts without any dip-hump characteristic (bottom panels Fig. 2d), unlike the spectra of the deflecting Xe- and CO-tips.

The effect of tip flexibility on the contrast formation

To investigate how the probe particle deflection affects the imaging performance in more detail, we performed contrast simulations by using a numerical model introduced by Hapala *et al.*[20] Considering tip deflection based on horizontal and vertical spring constants (k_h and k_v), it mechanically describes the tip apex as a combination of tip base and a suspended probe particle (insets in ESI Fig. S2†). Focusing on the case of the CO-tip, Fig. 3 compares simulated and experimental contrasts together with corresponding $\Delta f(Z)$-spectra. We find that the simulations largely reproduce the most distinct contrast features. In particular, this holds for the height-dependent contrast inversion at $\Delta Z \approx 0.4$ Å and the characteristic dip-hump evolution of the $\Delta f(Z)$-spectra. Hence, the pronounced tip bending at $\Delta Z \approx 1.6$ Å and below, the flexibility of the CO molecule dominates the contrast formation.[37] It is evident that the contrast inversion and the resulting spurious contrast at the inter AR-sites are closely related to artificial contrast features observed for flexible tips at locations with strongly varying tip–

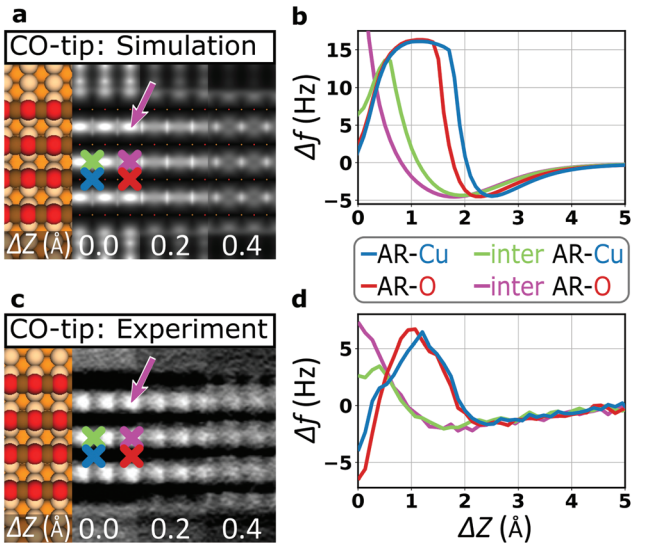

Fig. 3 Simulating contrast signatures due to tip flexibility. (a) Contrast simulation based on the probe particle model[20] using the electrostatic potential of a DFT-based structural model of an oxide stripe.[39] Horizontal and vertical spring constants for the CO-tip are also derived from DFT (k_h = 1.7 N m^{-1}, k_v = 326.9 N m^{-1}, ESI Fig. S3†). (b) Corresponding simulated background-subtracted $\Delta f(Z)$-spectra on various atomic sites (see color-coded crosses in (a)). (c) Constant-height AFM image recorded with a CO-tip as cut out from Fig. 2c for comparison with the simulation. (d) Experimental background-subtracted $\Delta f(Z)$-spectra recorded with the CO-tip. The simulation reproduces the contrast inversion and the related atomic corrugation at the inter-row sites (pink arrows in (a) and (c)).

sample potential, *e.g.* at intermolecular sites in organic nanostructures[23,25] or at protruding topographical features.[20,31,38]

Analyzing the atomic corrugation along the AR-direction below the point of contrast inversion, the atomic-scale protrusions can clearly be assigned to the inter added row sites between two AR-O atoms (pink arrows in Fig. 3). In a further step, we performed such simulations also by assuming the parameters for a Xe-tip where we obtained very similar results with excellent agreement between simulations and experiment (ESI Fig. S2†). Please note that CO- and the Xe-tips, both show the well-known contrast sharpening effect for flexible tips[7,20] (ESI Fig. S2†).

Comparing all DFT-derived lateral spring constants to quantify tip rigidity, the CuOx-tip is more than an order of magnitude stiffer than the Xe- and CO-tips (ESI Fig. S3†). As a result, the simulations assuming the parameters for a CuOx-tip do not show any indication of tip flexibility (ESI Fig. S2†). At the same time, the simulated $\Delta f(Z)$-spectra do not reproduce the differences in depth and shape of the spectral minima on the AR-Cu and AR-O sites (ESI Fig. S2†). This is a consequence of the applied model, which works excellently to catch the effects of mechanical tip relaxations, but does not include the fundamental chemical interactions between the tip and the surface.[32]

The effect of chemical interaction on the contrast formation

Since not all contrast features can be assigned to the tip flexibility, we also focused on the chemical interaction between the

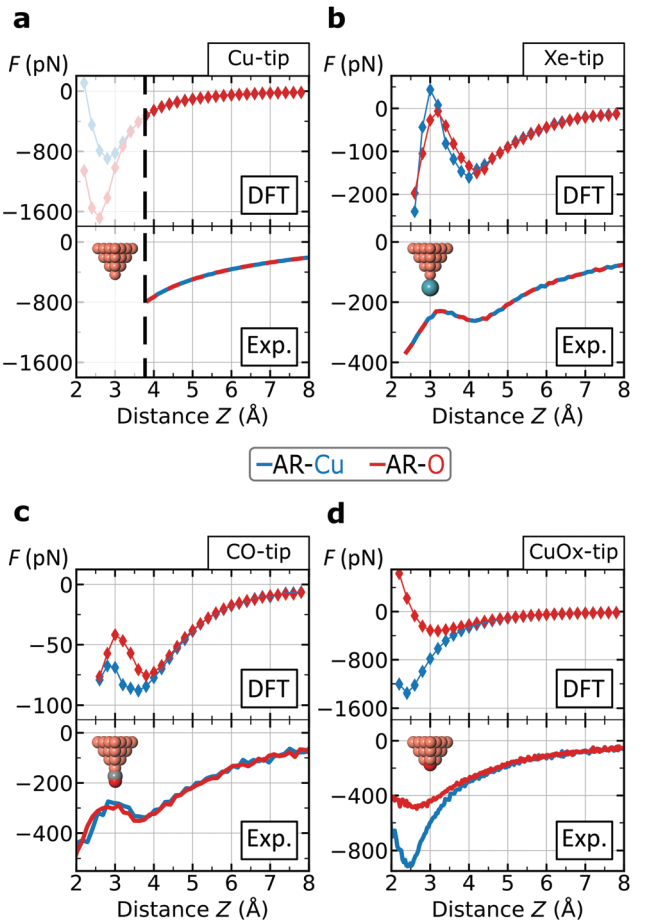

Fig. 4 Force–distance analysis on specific atomic surface sites. The curves represent the force interaction on the AR-Cu and AR-O sites for the four tips: (a) Metallic Cu-tip; (b) Xe-tip; (c) CO-tip; (d) CuOx-tip. The curves on top row are based on DFT-simulations and the experimental forces on the bottom are converted by the Sader–Jarvis algorithm[40] the corresponding $\Delta f(Z)$-spectra (facilitating comparability, without background subtraction). Theoretical and experimental spectra are roughly aligned by shifting the experimental curves along the ΔZ-scale. The black dashed line in frame (a) at $Z \approx 3.8$ Å marks the lower experimental limit for the Cu-tip where imaging becomes unstable, while the upper limit for a distinct contrast is at $Z \approx 3.5$ Å. For the Cu-, and Xe-tip the atomic sites are not distinguishable. In frame (c) the CO-tip simulation reveals a small range with a separated contrast around $Z \approx 3.2$ Å. All atoms of the surface were fixed during the simulation. The absolute height Z is defined as the vertical distance between the initial position of the tip-terminating atom and the center of AR-O atom.

tip and the surface atoms. The top row in Fig. 4 shows force–distance simulations based on DFT calculations for the AR-Cu- and AR-O sites for all tips. In the bottom row of Fig. 4, the corresponding experimental force curves are shown. Here the Z-scales are adjusted to the simulations by roughly aligning the positions of the force minima.

We find an excellent qualitative agreement for the general shapes of the force curves between simulation and experiment. In particular, the characteristic dip-hump evolution[37] and the related pronounced tip deflection (ESI Fig. S4†) is largely reproduced (Fig. 4b and c). To compare chemical reactivity for

the different sites and tips, we consider the maximum attraction, *i.e.* the depth of the force minimum. In fact, the DFT-simulated and experimental force curves of the Xe- and CO-tip, both exhibit only weakly pronounced minima, which confirms the chemical passivation of these tips.[13,18] Please note that this is particularly emphasized in the simulations when the van der Waals contribution is subtracted revealing almost no chemical attraction (ESI Fig. S5†).

The DFT-simulations for the Xe- and CO-tip in Fig. 4b and c show that the height-dependent interactions on the AR-Cu- and AR-O sites are very similar, which is in agreement with the experimentally observed weak contrast for these tips. The simulations for the Cu-tip show a pronounced separation for the two atomic sites below $Z \approx 3.5$ Å, however, as mentioned above, this height regime is not accessible in the experiment (dashed, vertical line in Fig. 4a). In contrast, both, the simulated and experimental force spectra for the CuOx-tip show a pronounced separation for the AR-Cu- and AR-O sites (Fig. 4d). Here we observe significantly deeper minima especially on the AR-Cu site, indicating a corresponding higher chemical reactivity. Due to the higher stiffness of the CuOx-tip (ESI Fig. S3†) this regime is experimentally accessible, which allows to obtain a distinct chemical contrast in this case. By subtracting the van der Waals contribution from the simulated CuOx-tip spectra the observed contrast features can be clearly assigned to an increased chemical attraction between the CuOx-tip and the AR-Cu site (ESI Fig. S5†).

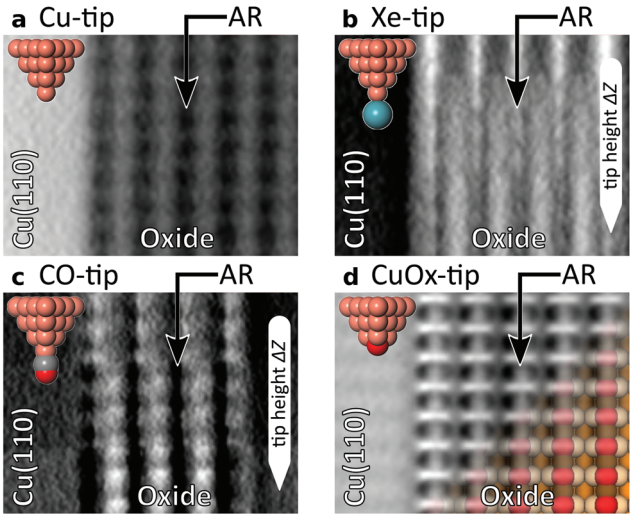

Fig. 5 Comparing most distinct contrasts in the experiments for each tip. (a) The Cu-tip allows imaging only in the attractive regime where the ARs appear as dark lines. (b) The Xe-tip shows the contrast inversion of five added rows for heights ΔZ from 0.4 Å to 0.0 Å. (c) For the CO-tip a slightly more pronounced atomic corrugation around the point of contrast inversion and below (0.6 Å to 0.2 Å) is observed. (d) The CuOx-tip reveals a remarkable shape distinction between the ellipsoid appearance of AR-Cu atoms and the sharp features on the AR-O sites. This facilitates a straight-forward atomic identification of AR-Cu and AR-O sites. The aligned model of the (2 × 1)O-reconstruction is fading into the experimental image. Color code of (2 × 1)O–Cu(110) model corresponds to Fig. 1b. Frame size of each image is 26 × 35 Å.

Conclusions

We compared the imaging and force-spectroscopy characteristics of four frequently used, atomically defined AFM tips on a partially oxidized Cu(110) surface. Investigating their performance in one specific experiment establishes direct comparability of the results. We found that the high reactivity of the Cu-tip leads to atomic relaxations within the tip–sample junction already in the attractive force regime. This results in sudden tip changes preventing to reach sufficient resolution for a detailed analysis of the surface atomic structure (Fig. 5a). The same experiment performed with the Xe- and CO-passivated tips, allows entering the repulsive force regime. Although this strongly emphasizes the ARs, the AFM contrast shows pronounced image distortions due to the high flexibility of these tips. Corresponding probe particle simulations show excellent agreement with our experimental data allowing to conclude that emerging contrast features at inter-atomic sites originate from dynamic bending effects. In fact, these bending effects and the suppressed chemical contrast hamper a clear distinction of the atomic sites within the oxide (Fig. 5b and c). In contrast, the CuOx-tip allows entering the repulsive force regime where it shows strongly site-specific interactions and a shape distinction (Fig. 5d), which facilitates the identification of atomic sites in the images. In this regard our study supports previous efforts to shift the focus of NC-AFM tip functionalization from organic adsorbates to inorganic surface systems.[41,42] Here, CuOx-tips could be especially promising for the characterization of metal–oxide surfaces and their catalytically active surface sites.[43–46]

Author contributions

H.M., S.A., and H.F. conceived the experiments. B.S.L., D.Y., and A.T. performed the experiments. B.S.L., D.Y., and H.M. analysed the data. B.S.L., and A.T. performed the probe particle simulations. Z.H., W.J., and S.A. performed the DFT-simulations. All authors discussed the results and commented on the manuscript drafted by B.S.L., and H.M.

Conflicts of interest

There are no conflicts to declare.

Acknowledgements

The authors gratefully acknowledge support by the Deutsche Forschungsgemeinschaft (DFG) through projects MO 2345/4-1, AM 460/2-1, and FU 299/19. Technical support was provided by Amala Elizabeth.

References

1 P. Ruffieux, S. Wang, B. Yang, C. Sánchez-Sánchez, J. Liu, T. Dienel, L. Talirz, P. Shinde, C. A. Pignedoli, D. Passerone, T. Dumslaff, X. Feng, K. Müllen and R. Fasel, *Nature*, 2016, **531**, 489–492.
2 L. Gross, B. Schuler, N. Pavliček, S. Fatayer, Z. Majzik, N. Moll, D. Peña and G. Meyer, *Angew. Chem., Int. Ed.*, 2018, **57**, 3888–3908.
3 K. Kaiser, L. M. Scriven, F. Schulz, P. Gawel, L. Gross and H. L. Anderson, *Science*, 2019, **365**, 1299–1301.
4 R. Pawlak, X. Liu, S. Ninova, P. D'Astolfo, C. Drechsel, J.-C. Liu, R. Häner, S. Decurtins, U. Aschauer, S.-X. Liu and E. Meyer, *Angew. Chem.*, 2021, **60**, 8370–8375.
5 A. J. Weymouth, T. Hofmann and F. J. Giessibl, *Science*, 2014, **343**, 1120–1122.
6 G. Czap, P. J. Wagner, F. Xue, L. Gu, J. Li, J. Yao, R. Wu and W. Ho, *Science*, 2019, **364**, 670–673.
7 L. Gross, F. Mohn, N. Moll, B. Schuler, A. Criado, E. Guitián, D. Peña, A. Gourdon and G. Meyer, *Science*, 2012, **337**, 1326–1329.
8 D. G. de Oteyza, P. Gorman, Y.-C. Chen, S. Wickenburg, A. Riss, D. J. Mowbray, G. Etkin, Z. Pedramrazi, H.-Z. Tsai, A. Rubio, M. F. Crommie and F. R. Fischer, *Science*, 2013, **340**, 1434–1437.
9 J. N. Ladenthin, T. Frederiksen, M. Persson, J. C. Sharp, S. Gawinkowski, J. Waluk and T. Kumagai, *Nat. Chem.*, 2016, **8**, 935–940.
10 R. Zuzak, R. Dorel, M. Kolmer, M. Szymonski, S. Godlewski and A. M. Echavarren, *Angew. Chem., Int. Ed.*, 2018, **57**, 10500–10505.
11 F. Huber, J. Berwanger, S. Polesya, S. Mankovsky, H. Ebert and F. J. Giessibl, *Science*, 2019, **366**, 235–238.
12 F. Albrecht, D. Rey, S. Fatayer, F. Schulz, D. Pérez, D. Peña and L. Gross, *Angew. Chem.*, 2020, **59**, 22989–22993.
13 L. Gross, F. Mohn, N. Moll, P. Liljeroth and G. Meyer, *Science*, 2009, **325**, 1110–1114.
14 J. Zhang, P. Chen, B. Yuan, W. Ji, Z. Cheng and X. Qiu, *Science*, 2013, **342**, 611–614.
15 M. Emmrich, F. Huber, F. Pielmeier, J. Welker, T. Hofmann, M. Schneiderbauer, D. Meuer, S. Polesya, S. Mankovsky, D. Ködderitzsch, H. Ebert and F. J. Giessibl, *Science*, 2015, **348**, 308–311.
16 S. Wickenburg, J. Lu, J. Lischner, H.-Z. Tsai, A. A. Omrani, A. Riss, C. Karrasch, A. Bradley, H. S. Jung, R. Khajeh, D. Wong, K. Watanabe, T. Taniguchi, A. Zettl, A. C. Neto, S. G. Louie and M. F. Crommie, *Nat. Commun.*, 2016, **7**, 13553.
17 F. J. Giessibl, *Rev. Sci. Instrum.*, 2019, **90**, 011101.
18 F. Mohn, B. Schuler, L. Gross and G. Meyer, *Appl. Phys. Lett.*, 2013, **102**, 073109.
19 A. M. Sweetman, S. P. Jarvis, H. Sang, I. Lekkas, P. Rahe, Y. Wang, J. Wang, N. R. Champness, L. Kantorovich and P. Moriarty, *Nat. Commun.*, 2014, **5**, 3931.
20 P. Hapala, G. Kichin, C. Wagner, F. S. Tautz, R. Temirov and P. Jelínek, *Phys. Rev. B: Condens. Matter Mater. Phys.*, 2014, **90**, 085421.
21 Q. Zhong, X. Li, H. Zhang and L. Chi, *Surf. Sci. Rep.*, 2020, **75**, 100509.
22 N. Moll, B. Schuler, S. Kawai, F. Xu, L. Peng, A. Orita, J. Otera, A. Curioni, M. Neu, J. Repp, G. Meyer and L. Gross, *Nano Lett.*, 2014, **14**, 6127–6131.
23 P. Hapala, M. Švec, O. Stetsovych, N. J. van der Heijden, M. Ondráček, J. van der Lit, P. Mutombo, I. Swart and P. Jelínek, *Nat. Commun.*, 2016, **7**, 11560.
24 H. Mönig, *Chem. Commun.*, 2018, **54**, 9874–9888.
25 S. K. Hämäläinen, N. van der Heijden, J. van der Lit, S. den Hartog, P. Liljeroth and I. Swart, *Phys. Rev. Lett.*, 2014, **113**, 186102.
26 H. Labidi, M. Koleini, T. Huff, M. Salomons, M. Cloutier, J. Pitters and R. A. Wolkow, *Nat. Commun.*, 2017, **8**, 14222.
27 H. Mönig, D. R. Hermoso, O. Díaz Arado, M. Todorović, A. Timmer, S. Schüer, G. Langewisch, R. Pérez and H. Fuchs, *ACS Nano*, 2016, **10**, 1201–1209.
28 A. Shiotari, T. Odani and Y. Sugimoto, *Phys. Rev. Lett.*, 2018, **121**, 116101.
29 M. Shekhirev, P. Zahl and A. Sinitskii, *ACS Nano*, 2018, **12**, 8662–8669.
30 A. Liebig and F. J. Giessibl, *Appl. Phys. Lett.*, 2019, **114**, 143103.
31 H. Mönig, S. Amirjalayer, A. Timmer, Z. Hu, L. Liu, O. Díaz Arado, M. Cnudde, C. A. Strassert, W. Ji, M. Rohlfing and H. Fuchs, *Nat. Nanotechnol.*, 2018, **13**, 371–375.
32 A. Liebig, P. Hapala, A. J. Weymouth and F. J. Giessibl, *Sci. Rep.*, 2020, **10**, 14104.
33 K. Kern, H. Niehus, A. Schatz, P. Zeppenfeld, J. Goerge and G. Comsa, *Phys. Rev. Lett.*, 1991, **67**, 855–858.
34 F. J. Giessibl, *Appl. Phys. Lett.*, 1998, **73**, 3956–3958.
35 M. Z. Baykara, M. Todorović, H. Mönig, T. C. Schwendemann, O. Ünverdi, L. Rodrigo, E. I. Altman, R. Pérez and U. D. Schwarz, *Phys. Rev. B: Condens. Matter Mater. Phys.*, 2013, **87**, 155414.
36 H. Mönig, M. Todorović, M. Z. Baykara, T. C. Schwendemann, L. Rodrigo, E. I. Altman, R. Pérez and U. D. Schwarz, *ACS Nano*, 2013, **7**, 10233–10244.
37 N. Néel and J. Kröger, *Nano Lett.*, 2021, **21**, 2318–2323.
38 N. Pavliček, B. Fleury, M. Neu, J. Niedenführ, C. Herranz-Lancho, M. Ruben and J. Repp, *Phys. Rev. Lett.*, 2012, **108**, 086101.
39 A. Timmer, H. Mönig, M. Uphoff, O. Díaz Arado, S. Amirjalayer and H. Fuchs, *Nano Lett.*, 2018, **18**, 4123–4129.
40 J. E. Sader and S. P. Jarvis, *Appl. Phys. Lett.*, 2004, **84**, 1801–1803.
41 M. Schneiderbauer, M. Emmrich, A. J. Weymouth and F. J. Giessibl, *Phys. Rev. Lett.*, 2014, **112**, 166102.
42 J. Onoda, M. Ondráček, P. Jelínek and Y. Sugimoto, *Nat. Commun.*, 2017, **8**, 15155.

43 M. Wagner, B. Meyer, M. Setvin, M. Schmid and U. Diebold, *Nature*, 2021, **592**, 722–725.
44 L. Egger, M. Hollerer, C. S. Kern, H. Herrmann, P. Hurdax, A. Haags, X. Yang, A. Gottwald, M. Richter, S. Soubatch, F. S. Tautz, G. Koller, P. Puschnig, M. G. Ramsey and M. Sterrer, *Angew. Chem.*, 2021, **60**, 5078–5082.
45 D. C. Grinter, M. Allan, H. J. Yang, A. Salcedo, G. E. Murgida, B.-J. Shaw, C. L. Pang, H. Idriss, M. V. Ganduglia-Pirovano and G. Thornton, *Angew. Chem.*, 2021, **60**, 13835–13839.
46 J. Hulva, M. Meier, R. Bliem, Z. Jakub, F. Kraushofer, M. Schmid, U. Diebold, C. Franchini and G. S. Parkinson, *Science*, 2021, **371**, 375–379.